



Plasmonic TiN boosting nitrogen-doped TiO₂ for ultrahigh efficient photoelectrochemical oxygen evolution

Yueying Li^a, Jian-Gan Wang^{a,*}, Yuancheng Fan^b, Huanhuan Sun^a, Wei Hua^a, Huanyan Liu^a, Bingqing Wei^{a,c,*}

^a State Key Laboratory of Solidification Processing, Center for Nano Energy Materials, School of Materials Science and Engineering, Northwestern Polytechnical University and Shaanxi Joint Lab of Graphene (NPU), Xi'an, 710072, China

^b Key Laboratory of Space Applied Physics and Chemistry, Ministry of Education and Department of Applied Physics, School of Science, Northwestern Polytechnical University, Xi'an, 710129, China

^c Department of Mechanical Engineering, University of Delaware, Newark, DE19716, USA

ARTICLE INFO

Keywords:

Plasmonic effect
TiO₂
Photoelectrochemical water splitting
TiN
Heterostructure

ABSTRACT

Achieving a high photocatalytic activity toward photoelectrochemical (PEC) water splitting has become a formidable challenge for titanium oxide (TiO₂) owing to its poor photoresponse to visible light and low electrical conductivity. Herein, we report the first demonstration of nonmetal TiN as a plasmonic booster to significantly enhancing the PEC water splitting performance of TiO₂. A unique multiscaled architecture organized by interweaving hollow microfiber monolith and hierarchical TiN/N-TiO₂ nanorod arrays is fabricated by a facile seamless nitridation process. The conductive TiN not only affords plasmon resonance on the N-TiO₂ to enable high photoactivity in a broadband UV–vis light region, but also assists in the charge generation-separation-transportation-injection efficiency of TiO₂ for enhanced water oxidation kinetics. The TiN/N-TiO₂ heterostructure manifests an unprecedented high and durable photocurrent density of 3.12 mA cm⁻² at 1.23 V (vs. reversible hydrogen electrode (RHE)) under standard AM 1.5 G illumination and substantiates an outstanding visible-light-driven photocurrent density of 1.63 mA cm⁻² without the use of any hole scavenger and cocatalysts. This study will enrich the fundamental understanding of nonmetal plasmonic effect in and beyond the field of PEC water splitting.

1. Introduction

Photoelectrochemical (PEC) water splitting represents a clean chemical energy conversion system that can reduce the global dependence on fossil fuels and mitigate the related environmental problems [1–4]. Semiconductor materials are the most indispensable component to determine PEC performance. Among the promising candidates, titanium dioxide (TiO₂) has been recognized as excellent photocatalysts for PEC water oxidation owing to its ideal band-edge positions, good photo-corrosion resistance, easy preparation, and low cost [5–7]. However, TiO₂ semiconductor is only photo-sensitive to the ultraviolet (UV) light because of its wide band gap of 3.2 eV [8,9]. To improve the solar energy conversion efficiency of TiO₂, it is imperative to extend the light absorption toward the visible light region, which accounts for 45% of the solar spectrum. For this purpose, a large number of studies have been devoted to exploring new strategies of hetero-atom doping, such

as nitrogen, [10–15] carbon [16,17], transition metal [18–21], and silicon [22]. In particular, nitrogen implantation is the most promising method, which could narrow the band gap of TiO₂ and thereof extends optical absorption up to a relatively high wavelength of 500 nm. In addition, it is equally important to note that TiO₂ is subjected to rapid electron-hole recombination rate due to its poor electrical conductivity. This issue can to some extent be addressed by co-catalyst sensitization as well as nitrogen doping. Co-catalyst sensitization could assist in increasing the PEC water splitting kinetics, but its surface coverage on TiO₂ also minimizes the effective light absorption [23–28]. By contrast, nitrogen doping is a reliable and feasible way to modify the electronic structure of TiO₂ by introducing oxygen vacancies and/or Ti³⁺ color centers [29]. Moreover, it is reported that the oxygen vacancies are capable of self-catalyzing water oxidation and decreasing the surface adsorption energy of water molecules for subsequent disassociation [30,31]. Despite these substantial progress, the visible light is still not

* Corresponding authors at: State Key Laboratory of Solidification Processing, Center for Nano Energy Materials, School of Materials Science and Engineering, Northwestern Polytechnical University and Shaanxi Joint Lab of Graphene (NPU), Xi'an, 710072, China.

E-mail addresses: wangjiangan@nwpu.edu.cn (J.-G. Wang), weib@udel.edu (B. Wei).

<https://doi.org/10.1016/j.apcatb.2019.01.044>

Received 28 November 2018; Received in revised form 12 January 2019; Accepted 16 January 2019

Available online 19 January 2019

0926-3373/ © 2019 Elsevier B.V. All rights reserved.

well utilized and the electronic conductivity enhanced by nitrogen doping is rather limited, thereby leaving a huge improvement space.

Plasmonics has recently emerged as a prominent light-trapping technology in the fields of photovoltaic devices, [32] photocatalysis [33–36], and surface-enhanced Raman scattering (SERS) [37,38]. The excitation and oscillation of free conduction electrons in plasmonic metals give rise to localized surface plasmon resonances, which can assist in strong light absorption and intense electric field enhancement [39]. Surface plasmonic effect is demonstrated to be capable of boosting charge carrier generation (i.e., electron-hole pairs) rate of semiconductor and promoting hot electron transfer from metal to semiconductor [40]. The conventional plasmonic materials include noble metals of gold and silver. Notably, these metals not only suffer from high-cost concern, but also have moderate electrical contact to the semiconductor due to the heterogeneous solution-processing chemical reduction method [41]. It should be worth to mention that the electrical contact is of great importance for hot electron transportation. Taking all these issues into consideration, developing low-cost plasmonic materials with an intimate electric connection to the semiconductor is highly desirable.

Some of nonmetal ceramics, such as metal nitrides, are of excellent metallic characteristics. In particular, titanium nitride (TiN) could exhibit good plasmonic behavior even with similar optical properties to gold in the optical range [42,43]. This inspires us to integrate the low-cost plasmonic TiN with nitrogen-doped TiO₂ (N-TiO₂) in this work. The bi-functional combination is anticipated to gain synergistic benefits of efficient visible light harvest and improved electrical conductivity for enhancing PEC performance. As a proof-of-concept, a freestanding cloth monolith with each hollow fiber assembled by TiN/N-TiO₂ nanorod arrays is fabricated, as illustrated in Fig. 1a. The integrated entity shares a cascade of advantages: (i) the nitrogen-doping and plasmonic effect enable an almost full-spectrum UV–vis light adsorption; (ii) the intimate electric connection between conductive TiN and N-TiO₂ accelerates the electron-hole generation and separation; (iii) the hollow fiber structure facilitates light scattering to increase photo path length; and (iv) the hierarchical nanorod arrays provide a large accessible surface area for electrocatalytic active sites. As a consequence, an unprecedented photocurrent density of 3.12 mA cm^{−2} at 1.23 V (vs. RHE) is achieved without any other cocatalysts under a standard AM 1.5 G solar spectrum. In addition, the TiN/N-TiO₂ hybrid exhibits outstanding visible-light-driven PEC performance (1.63 mA cm^{−2}). The present study opens up a new design strategy window by integrating nonmetal plasmonic materials with semiconductors for high efficient PEC water splitting.

2. Experimental methods

2.1. Materials synthesis

TiO₂ nanorod arrays were grown on carbon cloth via a seed-assisted hydrothermal method similar to the previous report [44]. Firstly, the commercial silk cloth (2.0 cm × 2.0 cm) were cleaned in the ultrasonic cleaning machine with acetone, distilled water, and ethanol successively. After being carbonized at 900 °C for 3 h with a heating rate of 5 °C min^{−1}, the carbon cloth (CC) was immersed into 0.1 M titanium (IV) chloride ethanol solution for 8 h and heated in a tube furnace at 450 °C for 30 min using a heating rate of 5 °C min^{−1} under N₂ atmosphere. Then, the seeded CC was loaded into a Teflon-lined stainless-steel autoclave (50 ml volume) containing a mixture of titanium n-butoxide (0.5 ml), concentrated hydrochloric acid (36.5%–38% by weight, (12 ml)), and deionized water (12 ml). The sealed autoclave was maintained at 150 °C for 5 h. After naturally cooling, the TiO₂ nanorod arrays/CC was rinsed with deionized water, dried in air, and calcined at 800 °C for 3 h using a heating rate of 1 °C min^{−1} to remove the CC template. Finally, the obtained TiO₂ cloth was treated at 700 °C for 3 h with a heating rate of 2 °C min^{−1} in an ammonia atmosphere to

acquire the TiN/N-TiO₂ hierarchical nanorod arrays.

2.2. Characterization

XRD patterns were recorded using an X-ray diffractometer (Shimadzu XRD-7000 with Cu Kα radiation). The microstructures of the samples were characterized on a transmission electron microscopy (TEM, FEI Talos F200X) and a field emission scanning electron microscopy (FESEM, FEI Nano SEM 450) equipped with EDX system. Raman spectra were determined on a Renishaw Invia Raman microscope (laser wavelength: 532 nm) at room temperature. The X-ray photoelectron spectroscopy (XPS) was conducted on an XPS analysis (Physical Electronics PHI-5802) equipped with a monochromatic Al Kα X-ray source in an ultrahigh vacuum environment. The binding energy was calibrated using the C 1 s photoelectron peak at 284.8 eV as a reference. UV–vis absorption spectra were recorded on a UV–vis spectrophotometer (Perkin-Elmer Lambda 35).

2.3. Photoelectrochemical measurements

For the PEC measurements, a 300 W xenon lamp equipped with an AM 1.5 G filter was used as the light source. The light intensity is calibrated to be 100 mW cm^{−2} with a solar power meter (Beijing Perfect Technology Co. Ltd). The visible light irradiation was realized with a 420 nm cut-off filter. The PEC characterization was performed in a typical three-electrode configuration connected to an electrochemical workstation (CHI 760E, CH Instruments, China) with 1.0 M NaOH aqueous solution (pH = 13.6) as the electrolyte. The PEC reactor consisted of a photoanode, an Ag/AgCl (saturated KCl) electrode, and a Pt plate (1 cm × 2 cm) as working, reference, and counter electrodes, respectively. Hierarchical TiN/N-TiO₂ cloth (exposed area: 0.3 cm²) was directly employed as a photoanode. The electrolyte was purged with N₂ for 30 min to remove the dissolved oxygen before measurements. The typical linear sweep voltammogram (LSV) curves were measured at a scan rate of 10 mV/s in the forward direction. The electrochemical impedance spectroscopy (EIS) was performed in the frequency range from 10⁵ to 0.1 Hz with an amplitude of 10 mV under light irradiation. The incident photon-to-current conversion efficiency (IPCE) spectra were tested under monochromatic irradiation from a 300 W Xe lamp equipped with an optical filter at 1.23 V versus RHE, based on the equation:

$$\text{IPCE} = 1240 \times I / (\lambda \times P(\lambda))$$

where λ is the incident-light wavelength (nm), I is the measured photocurrent density (mA/cm²) under the monochromatic light, and $P(\lambda)$ is the power density of each wavelength (mW/cm²).

The measured potentials versus Ag/AgCl were converted to the RHE scale via the Nernst equation:

$$E_{\text{RHE}} = E_{\text{Ag/AgCl}} + 0.0591 \times \text{pH} + E^{\circ}_{\text{Ag/AgCl}}$$

where E_{RHE} is the converted potential versus RHE, $E_{\text{Ag/AgCl}}$ is the experimentally measured potential against the Ag/AgCl reference electrode, and $E^{\circ}_{\text{Ag/AgCl}} = 0.1976$ V at 25 °C.

2.4. Numerical simulation

Commercial Comsol Multiphysics was used for simulating the electric field distributions of the TiN/N-TiO₂ nanorod by a finite element method. The 3D simulation model was built by aligning a short TiN nanorod (diameter: 50 nm, length: 100 nm) on the TiO₂ nanorod. The incident laser wavelength was set in the range of 300–900 nm with a polarization direction along the x-axis. The electric field distributions were monitored at the crossover interfaces of TiN/N-TiO₂ in the y-z plane.

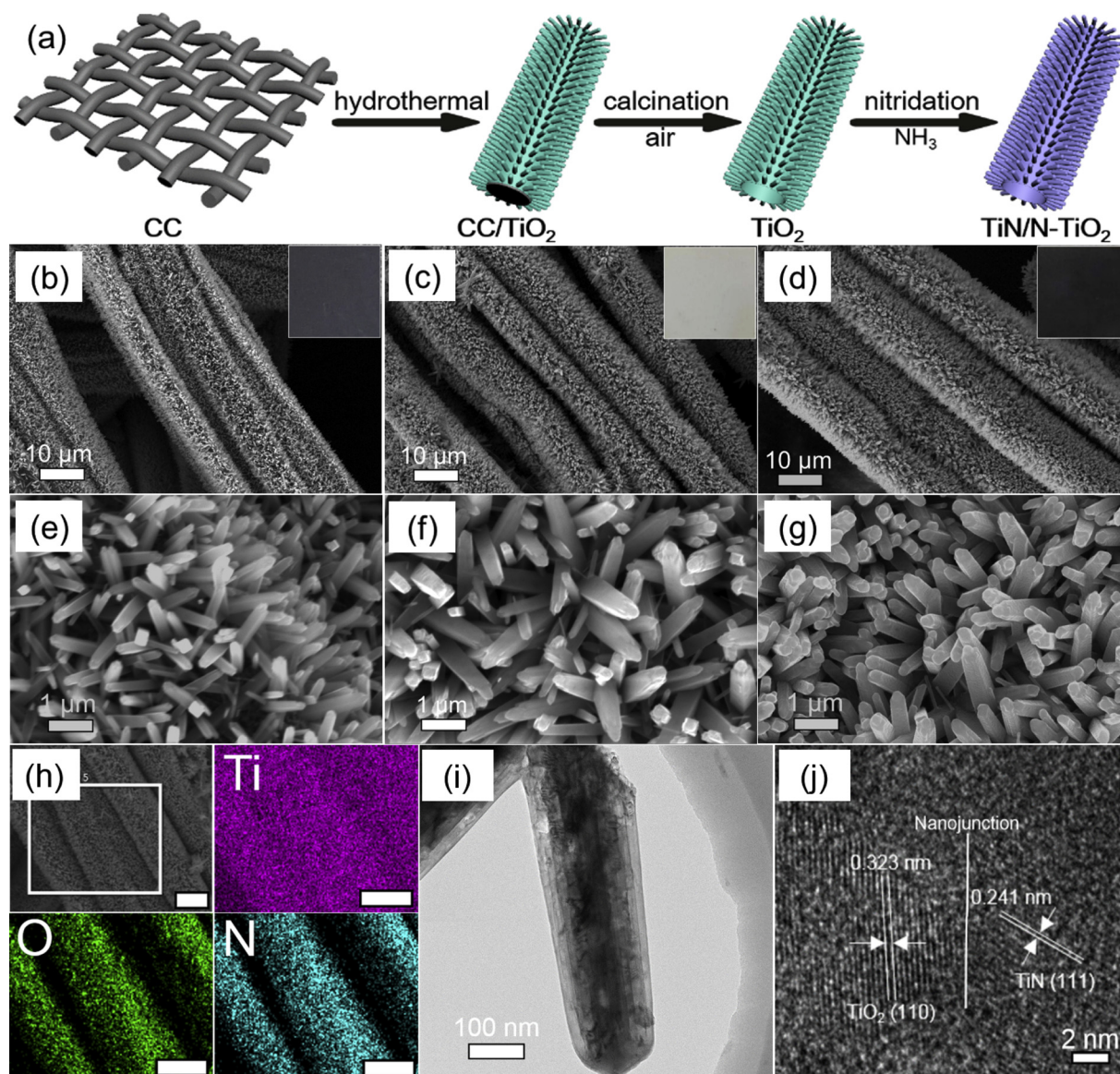


Fig. 1. (a) Schematic illustration of the synthetic process of TiN/N-TiO₂ hierarchical nanorod arrays; SEM images of (b, e) CC/TiO₂, (c, f) TiO₂ and (d, g) TiN/N-TiO₂; (h) EDX elemental mapping images, (i) TEM image and (j) HR-TEM image of TiN/N-TiO₂.

3. Results and discussion

Fig. 1a schematically illustrates the fabrication process of the TiN/N-TiO₂ hybrid structure. Carbon cloth (CC) was used as a three-dimensional (3D) porous matrix scaffold to support TiO₂ nanorod arrays through a simple hydrothermal growth method. The TiO₂-enwrapped CC was calcined at a high temperature in air to remove the carbon microfiber cores and increase the TiO₂ crystallinity. Finally, the hollowly-structured microfiber organized by hierarchical TiO₂ nanorod arrays was conducted by a post-thermal nitridation treatment, leading to the formation of the multiscaled TiN/N-TiO₂ heterostructures. Notably, the design strategy allows for high-temperature treatment (> 800 °C) without structural change owing to the robust freestanding interwoven nature. The merit is advantageous to the conventional conductive FTO supports, which suffer from chemical degradation under high temperature over 500 °C.

Fig. 1b–g show the detailed scanning electron microscopy (SEM) morphology evolution during the whole fabrication processes. The surface-smooth carbon microfiber (**Fig. S1a, b**) is uniformly and conformally wrapped by hierarchical building blocks of single-crystalline

TiO₂ nanorods (**Fig. 1b, e** and **Fig. S2**). After the oxidative calcination, the radially-grown TiO₂ nanorods are well maintained while the carbon microfiber cores are eliminated, thus constructing a unique hollow architecture (**Fig. 1c, f** and **S1f**). The subsequent nitridation process does not change the multiscaled hierarchical architecture (**Fig. 1d, g**). The diameter of the nanorods is about 180 nm and the corresponding length is estimated to be 1–1.5 μm from the cross-section of the fiber (**Fig. S1 h**). More interestingly, the color of the fabric is changing from grey black to white after removing the carbon fibers, and finally to dark black after nitridation (inset in **Fig. 1a–c**). The color evolution demonstrates the significant change of the optical properties of the nanorod structures. In particular, the dark black color of the TiN/N-TiO₂ fabric indicates a strong full-spectrum light trapping of the solar light, which will be elucidated in the following light absorption part. The energy-disperse X-ray (EDX) mapping of TiN/N-TiO₂ confirms the existence of the Ti, O, and N elements in the hybrid structure (**Fig. 1h**). **Fig. 1i** displays a representative transmission electron microscopy (TEM) image of a stick of heterostructured TiN/N-TiO₂ nanorod. The diameter is about 180 nm, which is in line with the SEM results (**Fig. 1g**). The high-resolution TEM image exhibits lattice fringes with

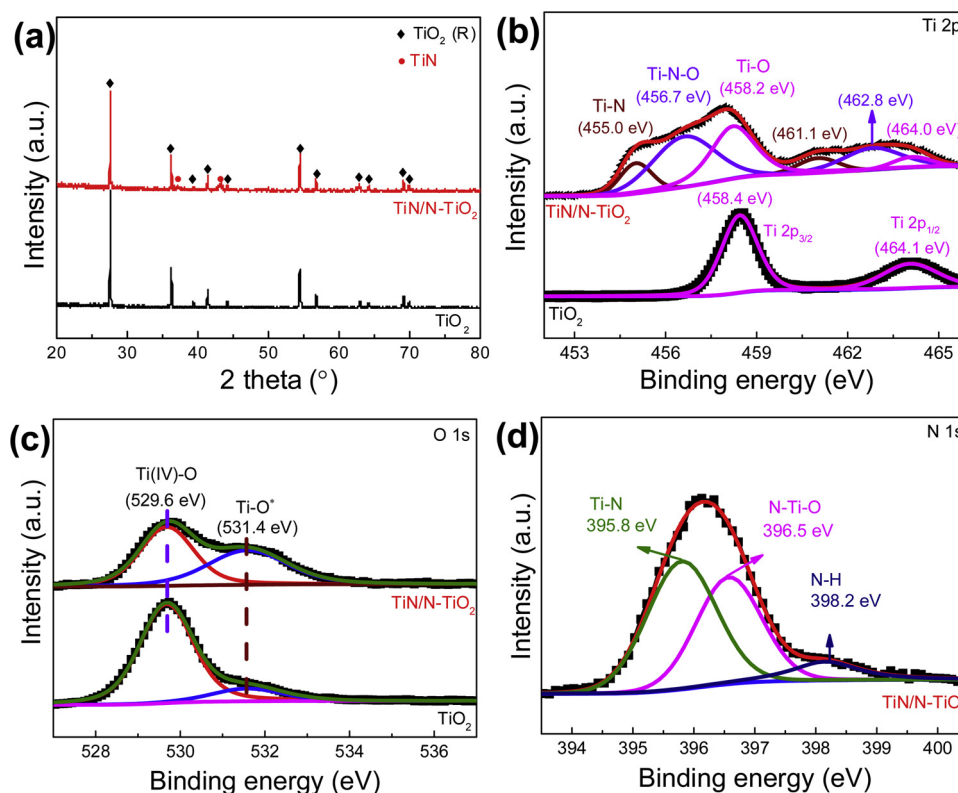


Fig. 2. (a) XRD patterns, (b) Ti 2p and (c) O 1s spectra of TiO₂ and TiN/N-TiO₂; (d) N 1s spectra of TiN/N-TiO₂.

interplanar distances of 0.323 and 0.241 nm, which belong to the TiO₂-(110) and TiN-(111) facets, respectively (Fig. 1j) [45,46].

The crystallographic structures of the as-fabricated fabrics are examined by X-ray diffraction (XRD). As shown in Fig. 2a, the calcined TiO₂ fabric is composed of a set of diffraction peaks of tetragonal rutile phase (JCPDS # 21-1276) without a trace of impurities. After subjecting to nitridation, in addition to the pristine pattern of TiO₂, two new diffraction peaks centered at 36.9° and 43.1° appear, which are characteristic of (111) and (200) crystal planes of TiN, respectively [47,48]. The XRD results indicate the successful formation of the hybrid TiN/N-TiO₂ heterostructure, which is further confirmed by the Raman spectra (Fig. S3). X-ray photoelectron spectroscopy (XPS) is carried out to investigate the surface chemistry of the samples. In stark contrast to the TiO₂ sample, the full-scan XPS spectrum of the TiN/N-TiO₂ sample (Fig. S4) manifests a strong signal of elemental N except for the common Ti and O elements. The high nitrogen incorporation agrees well with the EDX mapping. The chemical states of the elements are systematically studied by core-level XPS spectra. The TiO₂ sample exhibits a typical Ti 2p doublet peak of Ti–O bonds. In sharp contrast, the Ti 2p spectrum of the TiN/N-TiO₂ sample can be readily fitted by three components of Ti–N, Ti–N–O, and Ti–O bonds (Fig. 2b). The presence of Ti–N–O linkages indicates a strong electronic interaction between TiN and TiO₂. For the O 1s spectrum (Fig. 2c), the peak at 529.6 eV is typical Ti(IV)–O bonds, and the shoulder peak at 531.4 eV is associated with the Ti–O* species. The Ti–O* species are indicative of defect sites with a low oxygen coordination (i.e., oxygen vacancies (O*) or low valence Ti³⁺). It is important to note that the intensity of the Ti–O* species in the TiN/N-TiO₂ hybrid is much higher than that in the pure TiO₂, indicating a larger amount of defects in the hybrid. The defects have been demonstrated to have several advantages in the PEC catalysis by: (i) modulating the electron distribution to increase the electronic conductivity of TiO₂; [49] (ii) narrowing the band gap of TiO₂ to enable visible light photoactivity; [50] and (iii) lowering the surface adsorption energy barriers of water molecules to afford enhanced electrocatalytic activity for water splitting [51]. The N 1s

spectrum (Fig. 2d) can be deconvoluted into N–Ti–O component in the N–TiO₂, N–Ti component in the TiN phase, and adsorbed N [52].

The PEC measurement was carried out in a three-electrode electrochemical system using the freestanding fabric and 1.0 M NaOH as the working electrode and electrolyte, respectively. For comparison, the effect of nitrogen implantation is investigated by controlling the nitridation temperature in the range of 600–900 °C. Fig. 3a and Fig. S5 exhibit the linear sweep voltammogram (LSV) profiles of TiN/N-TiO₂ hybrid and pristine TiO₂ under simulated AM 1.5 G illumination and dark condition. It is noticeable that the TiN/N-TiO₂ hybrid electrode prepared at 700 °C shows the best photoactivity under illumination, which delivers an unprecedented photocurrent density as high as 3.12 mA cm^{−2} at 1.23 V vs. RHE without any hole scavengers and co-catalysts. The PEC performance is far superior to that of the pristine TiO₂ (0.76 mA cm^{−2}). More encouragingly, the photocurrent density, to the best of our knowledge, is a record value among the TiO₂-based photocatalysts. Table S1 summarizes the recent PEC properties of various TiO₂-based photocatalysts. The TiN/N-TiO₂ hybrid exceeds the previously best-reported materials, such as H-TiO₂ (2.50 mA cm^{−2}), [53] Co₃O₄/TiO₂/Si (2.71 mA cm^{−2}), [28] and Fe-TiO₂ (2.91 mA cm^{−2}) [21]. Further increasing the nitridation temperature would reduce the PEC activity (Fig. S5). This phenomenon can be attributed to fast carrier recombination induced by excess amount of TiN phase. The photoconversion efficiency (η) at various applied potentials is calculated according to the equation of $\eta = I(1.23\text{-V})/J_{\text{light}}$. Here, *I*, *V*, and *J_{light}* correspond to the photocurrent density (mA cm^{−2}), the applied potential (V), and light irradiance intensity (i.e., 100 mW cm^{−2} in this work). [22] Fig. 3b plots the resulting efficiency as a function of applied potential. The TiN/N-TiO₂ hybrid shows a much lower onset potential of 0.28 V and the photoconversion efficiency is greatly outperforming that of the pristine TiO₂ in the whole potential range. The maximum optical conversion efficiency is achieved at 0.68 V, indicating that the hybridization of TiN and N-TiO₂ is effective to enhance the PEC performance.

The photoactivity and chemical stability of the electrodes are

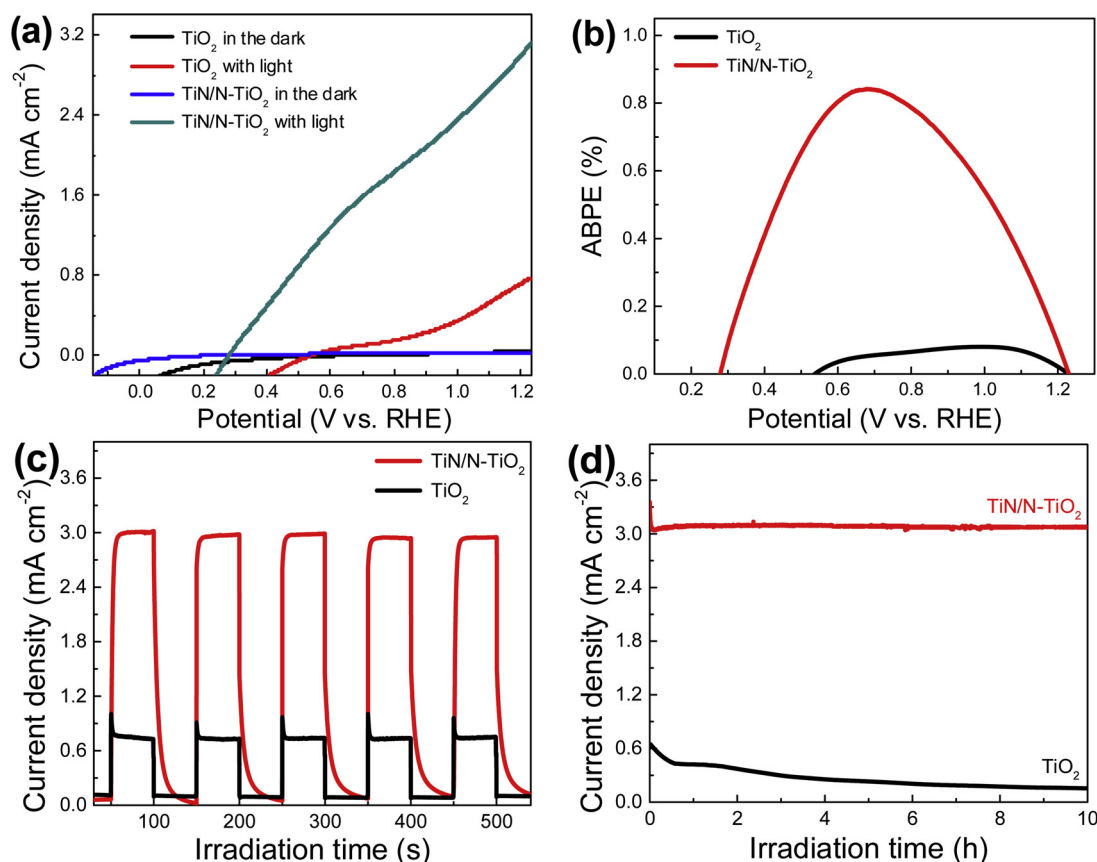


Fig. 3. (a) LSV curves, (b) Applied bias photon-to-current efficiency (ABPE) curves, (c) Photocurrent density for repeated on/off cycles and (d) long-term stability of TiO_2 and TiN/N-TiO_2 .

evaluated by photocurrent-time test at 1.23 V vs. RHE. As shown in Fig. 3c, the TiN/N-TiO_2 hybrid shows a rapid current response to the light switch, further confirming its high photoactivity. The photocurrent density is stable without noticeable degradation after five light on/off cycles. Fig. 3d displays long-term photoelectrochemical stability. In sharp contrast to the pristine TiO_2 , there is no obvious decrease in the photocurrent density for the TiN/N-TiO_2 hybrid electrode during the PEC water splitting reaction, indicating robust structural and chemical stability of the hybrid. We examined the morphology and XRD pattern of the hybrid after the long-term test. As shown in Figs. S6 and S7, the fiber-like morphology assembled by the hierarchical nanorod arrays are well preserved, and the phase structures are identical to the original ones (Fig. 2a). These observations demonstrate that the TiN/N-TiO_2 hybrid possesses excellent resistance to photocorrosion.

To rationalize the enhanced PEC performance of the TiN/N-TiO_2 hybrid, we first measured the UV-vis absorption properties. As shown in Fig. 4a, the pristine TiO_2 shows a narrow UV light absorption range below 400 nm due to its wide band gap (3.0 eV for rutile phase). For the TiN/N-TiO_2 hybrid, the light absorption edge of TiO_2 is extended to the visible light range at about 510 nm due to the nitrogen incorporation, which is in good accordance with the previously-reported N-TiO_2 [54]. The light absorption extension enables the N-TiO_2 to show good visible-light-driven PEC performance. More notably, the TiN/N-TiO_2 hybrid exhibits additional visible light absorption in the range of 550–900 nm resulting from the plasmonic absorption of TiN [42]. This demonstrates that the hybrid could utilize the full-spectrum UV-vis light, which is believed to be highly responsible for the enhanced PEC performance. To further reveal the optical properties of the hybrid, we simulate the light absorption curve by coupling plasmonic TiN and TiO_2 (Fig. S8). The simulated curve is very similar to the experimental one. Fig. 4b exhibits the electric field distribution surrounding the TiN nanoparticles under

various light wavelength. The localized surface plasmon resonance enables strong electric field enhancements at the TiN/TiO_2 crossover interfaces in the light range of 600–900 nm, thereby broadening the visible light absorption for better PEC water splitting.

To further unveil the intrinsic mechanism of the enhanced PEC performance of TiN/N-TiO_2 , incident photo-to-current efficiency (IPCE) was measured at 1.23 V vs. RHE in the wavelength range of 300–800 nm. As displayed in Fig. 4c, the IPCE values of the hybrid photoanode are far superior to that of the pristine TiO_2 counterpart over the whole spectra range. It is worth noting that the TiN/N-TiO_2 hybrid shows much higher IPCE values than the controlled TiO_2 in the visible light region (420–800 nm), indicating strong visible light harvesting capability of the TiN/N-TiO_2 hybrid. To confirm it, the photoanodes were again measured to obtain their LSV curves under visible light illumination ($\lambda > 420$ nm). Impressively, as shown in Fig. 4d, the TiN/N-TiO_2 hybrid could deliver a high visible-light-driven photocurrent density of 1.63 mA cm^{-2} at 1.23 V vs. RHE, which is much higher than that of the reported decorated TiO_x (1.4 mA cm^{-2}), [30] N-TiO_2 (0.83 mA cm^{-2}), [54] Fe-TiO_2 (0.94 mA cm^{-2}), [21] C/N-TiO_2 (0.62 mA cm^{-2}), [16] and Co-assisted N-TiO_2 nanowire (0.61 mA cm^{-2}) [15]. The high photocurrent also suggests that the visible light makes a significant contribution of ~50% to the overall performance.

Electrochemical impedance spectroscopy (EIS) was employed to attain an insight into the PEC reaction kinetics. The Nyquist plots (Fig. 5a) can be analyzed by the equivalent circuit model (inset), in which R_s , $R_{\text{transport}}$, and R_{transfer} represent external circuit resistance, the electron transport resistance of semiconductor, and the charge transfer resistance of PEC reaction occurred at the electrode/electrolyte interface [31]. Table S2 summarizes the fitting parameters. It is noted that the TiN/N-TiO_2 hybrid exhibits much lower R_s , $R_{\text{transport}}$, and R_{transfer} values than that of the pristine TiO_2 , indicating faster charge transfer

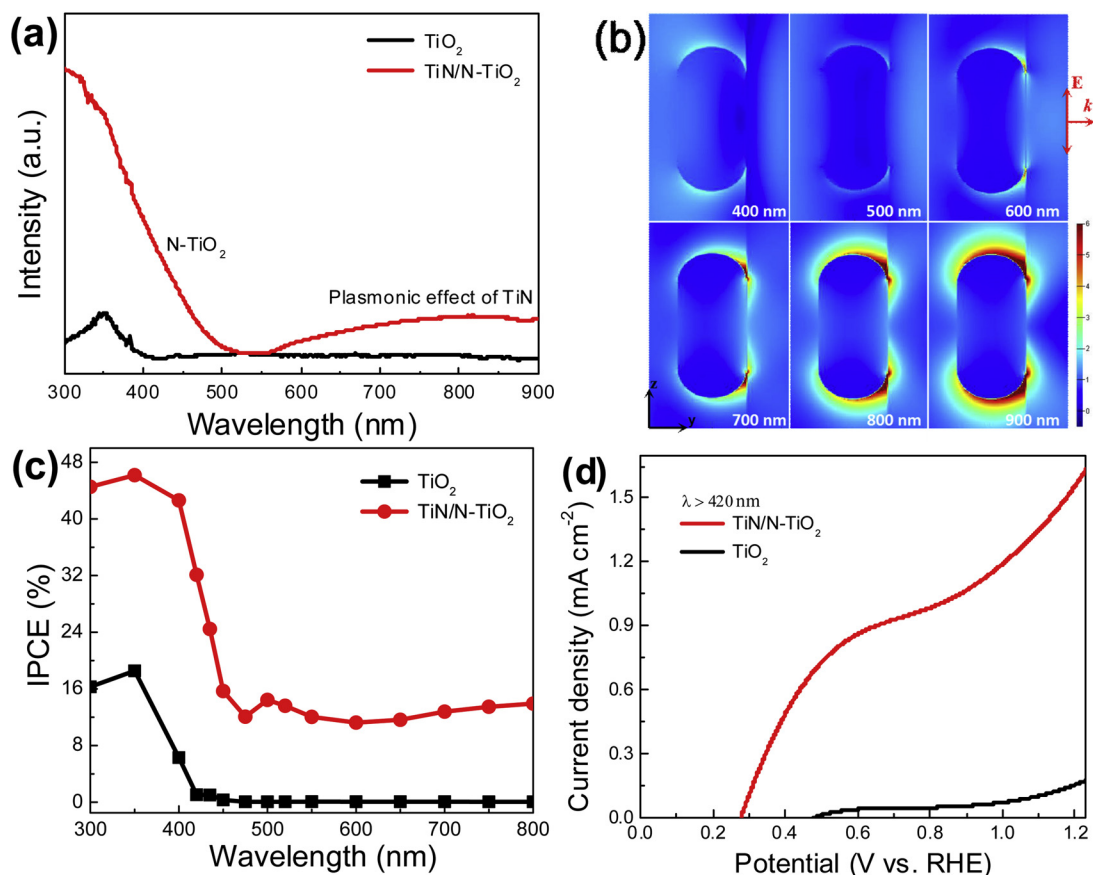


Fig. 4. (a) UV–vis absorption spectra of the TiO₂ and TiN/N-TiO₂. (b) Electric field distributions across the TiN/N-TiO₂ heterostructures. (c) IPCE plots and (d) LSV curves under visible light irradiation ($\lambda > 420$ nm) of TiO₂ and TiN/N-TiO₂.

kinetics. In addition, it is well-known that an increase of donor density in semiconductor leads to more efficient charge separation. The carrier density (N_d) can be calculated by the Mott-Schottky plot (Fig. 5b) based on the equation of $N_d = (2/e_0\epsilon\epsilon_0)[d(1/C^2)/dV]^{-1}$, where e_0 , ϵ , ϵ_0 , and V correspond to electron charge, dielectric constant of TiO₂ (170), vacuum permittivity, and applied electrode potential [53]. The positive slope of both plots is characteristic of an n-type semiconductor. The significantly shallower slope of the TiN/N-TiO₂ hybrid (1.6×10^9) reveals a higher carrier density of 5.1×10^{22} , which is 19 times larger than that of the pristine TiO₂ (2.7×10^{21}). The increased carrier density of the hybrid is ascribed to the presence of oxygen vacancies (electron donors, Fig. 2c) [16]. Moreover, the higher carrier density is also beneficial for the upward shift of the TiO₂ Fermi level toward conduction band and thereof enhanced charge separation efficiency [53].

In addition to the desirable characteristics of light absorption, charge separation, and charge transfer, the charge injection efficiency is another important metric for the overall PEC water splitting. To quantify the charge injection efficiency ($\eta_{\text{injection}}$), Na₂SO₃ (1.0 M) was added in the 1.0 M NaOH electrolyte as the hole scavenger. The $\eta_{\text{injection}}$ can be calculated through the relationship $\eta_{\text{injection}} = J_{\text{H}_2\text{O}}/J_{\text{sulfite}}$, where J_{sulfite} is the photocurrent density for sulfite oxidation [8]. Fig. S9 compares the LSV curves of the electrodes in electrolytes with and without the addition of Na₂SO₃. The photoresponse of the sulfite oxidation shows similar behavior to the water oxidation. Fig. 5c presents the charge injection efficiency of the electrodes. The TiN/N-TiO₂ hybrid electrode manifests a huge improvement in the charge injection efficiency relative to the pristine TiO₂, implying that the hybrid owns better intrinsic electrocatalytic activity toward water oxidation. The as-fabricated electrodes were also evaluated as the catalysts for oxygen evolution reaction (OER) without light illumination. As shown in Fig.

S10, the hybrid electrode requires lower overpotentials to drive the same current densities, further corroborating the better intrinsic electrocatalytic activity. Furthermore, the electrochemically active surface area (ECSA) can be determined from electrochemical double-layer capacitance (C_{dl}) [55]. By measuring the cyclic voltammogram (CV) curves in the potential range without Faradaic reactions (Fig. S11), we can obtain a linear relationship between the double layer charging current ($j_{\text{anode}} - j_{\text{cathode}}$) and the scan rate (ν). The C_{dl} or ECSA is half of the linear slope [56]. As displayed in Fig. 5d, the C_{dl} of the hybrid electrode ($581 \mu\text{F cm}^{-2}$) doubles that of the pristine TiO₂ ($270 \mu\text{F cm}^{-2}$), suggesting a higher ECSA with more effective active sites for OER. The higher ECSA of the hybrid is primarily from the oxygen vacancies caused by nitrogen incorporation.

On the basis of the above discussions, the substantial enhancement mechanism of PEC water splitting performance of the TiN/N-TiO₂ photoanode is proposed in Fig. 5e. Firstly, the hybrid TiN/N-TiO₂ could make a full harvest of the broad UV–vis light by nitrogen-doping and plasmonic effect. Secondly, the hollow fiber structure could extend the photon path length to strengthen the light trapping by scattering. And accordingly, the high light utilization and photoactivity excite a large number of electron-hole carrier pairs in the photoanode upon simulated sunlight illumination. Thirdly, the highly conductive TiN and the unique 1D geometric configuration could promote the electron transfer capability and thus accelerate the electron-hole separation efficiency. Subsequently, the photogenerated electrons migrate to the counter electrode for water reduction reaction. Meanwhile, the photogenerated holes transfer to the surface of photoanode for water oxidation reaction. It should be worth noting that the water oxidation kinetics is further enhanced by two factors: (i) the hierarchical nanorod arrays provide sufficient ion transport channels for building electro-active electrolyte/electrode interfaces effectively, and (ii) the oxygen vacancies in the N-

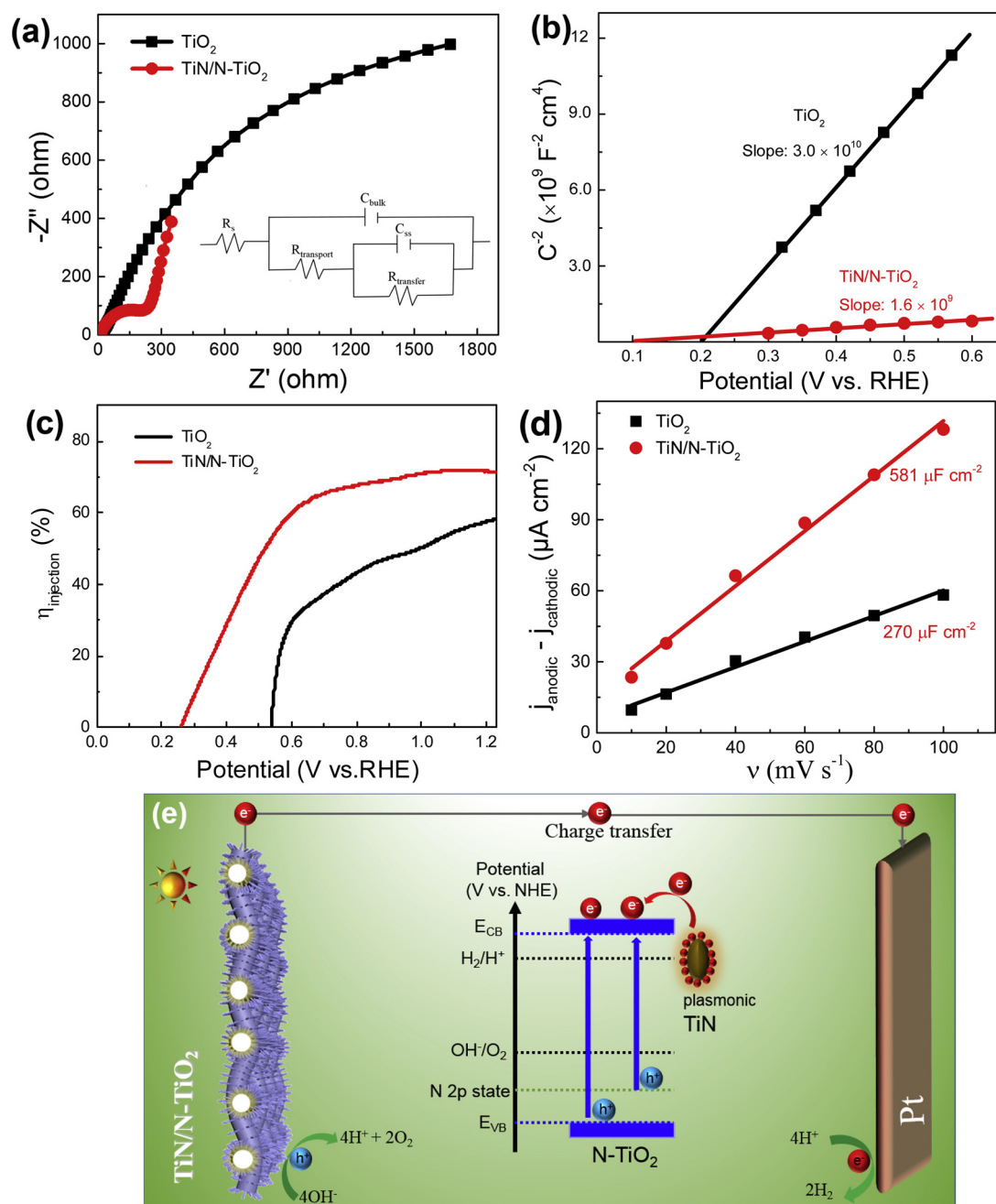


Fig. 5. (a) Nyquist plots at 1.23 V vs. RHE under light illumination, (b) Mott-Schottky plots, (c) Charge injection efficiency as a function of potential, and (d) Current density as a function of the scan rate for TiO₂ and TiN/N-TiO₂. (e) Schematic mechanism of the TiN/N-TiO₂ fabric boosting the PEC water splitting.

doped TiO₂ are of great beneficial in increasing the ECSA and the intrinsic electrocatalytic reactivity of active sites by efficient charge injection. Consequently, the TiN/N-TiO₂ photoanode manifests a record PEC overall current density without the assistance of any hole scavenger and cocatalysts.

4. Conclusions

In summary, we for the first time demonstrate the significant plasmonic effect of nonmetal TiN on boosting the PEC water splitting of TiO₂. To this end, 3D multiscaled monolith assembled by interweaving hollow microfibers and hierarchically heterostructured TiN/N-TiO₂ nanorod arrays has been constructed successfully by a seamless nitridation method. The unique hybrid architecture enables broadband UV–vis light harvesting capability and high-efficient charge generation-

separation-transportation-injection process. An unprecedented high and durable photocurrent density of 3.12 mA cm⁻² at 1.23 V (vs. RHE) under AM 1.5 G illumination is achieved without the use of any hole scavenger and cocatalysts. In particular, the combination of plasmonic effect and nitrogen implantation bestows the TiN/N-TiO₂ hybrid with outstanding visible light photoactivity, driving a superior photocurrent density of 1.63 mA cm⁻². The present study offers exciting new insight into integrating nonmetal plasmonic materials with suitable semiconductors for significantly enhanced PEC water splitting performance, and may extend to other fields of photocatalysis and solar cells.

Acknowledgements

The authors thank the research funds of National Natural Science Foundation of China (51772249, 51472204), Fundamental Research

Funds for the Central Universities (G2017KY0308), Natural Science Foundation of Shannxi Province (2018JM5092), Innovation Foundation for Doctor Dissertation of Northwestern Polytechnical University (CX201807), Hong Kong Scholars Program (XJ2017012), and Program of Introducing Talents of Discipline to Universities (B08040).

Appendix A. Supplementary data

Supplementary material related to this article can be found, in the online version, at doi:<https://doi.org/10.1016/j.apcatb.2019.01.044>.

References

- [1] C. Li, Z. Luo, T. Wang, J. Gong, Surface, bulk, and interface: rational design of hematite architecture toward efficient photo-electrochemical water splitting, *Adv. Mater.* (2018) 1707502–1707524.
- [2] Y. Yang, S. Niu, D. Han, T. Liu, G. Wang, Y. Li, Progress in developing metal oxide nanomaterials for photoelectrochemical water splitting, *Adv. Energy Mater.* (2017) 1700555–1700580.
- [3] S. Kment, F. Riboni, S. Pausova, L. Wang, L. Wang, H. Han, Z. Hubicka, J. Krysa, P. Schmuki, R. Zboril, Photoanodes based on TiO_2 and $\alpha\text{-Fe}_2\text{O}_3$ for solar water splitting-superior role of 1D nanoarchitectures and of combined heterostructures, *Chem. Soc. Rev.* 46 (2017) 3716–3769.
- [4] T. Hisatomi, J. Kubota, K. Domen, Recent advances in semiconductors for photocatalytic and photoelectrochemical water splitting, *Chem. Soc. Rev.* 43 (2014) 7520–7535.
- [5] B. Roose, S. Pathak, U. Steiner, Doping of TiO_2 for sensitized solar cells, *Chem. Soc. Rev.* 44 (2015) 8326–8349.
- [6] C. Lee, A. Taylor, S. Beirne, G. Wallace, 3D-printed conical arrays of TiO_2 electrodes for enhanced photoelectrochemical water splitting, *Adv. Energy Mater.* 7 (2017) 1701060–1701065.
- [7] T. Butburee, Y. Bai, H. Wang, H. Chen, Z. Wang, G. Liu, J. Zou, P. Khemthong, G. Max Lu, L. Wang, 2D porous TiO_2 single-crystalline nanostructure demonstrating high photo-electrochemical water splitting performance, *Adv. Mater.* (2018) 1705666–1705673.
- [8] F. Wu, Y. Yu, H. Yang, L. German, Z. Li, J. Chen, W. Yang, L. Huang, W. Shi, L. Wang, X. Wang, Simultaneous enhancement of charge separation and hole transportation in a TiO_2 - SrTiO_3 core-shell nanowire photoelectrochemical system, *Adv. Mater.* (2017) 1701432–1701438.
- [9] I. Cho, Z. Chen, A. Forman, D. Kim, P. Rao, T. Jaramillo, X. Zheng, Branched TiO_2 nanorods for photoelectrochemical hydrogen production, *Nano Lett.* 11 (2011) 4978–4984.
- [10] L. Sun, J. Cai, Q. Wu, P. Huang, Y. Su, C. Lin, N-doped TiO_2 nanotube array photoelectrode for visible-light-induced photoelectrochemical and photoelectrocatalytic activities, *Electrochim. Acta* 108 (2013) 525–531.
- [11] H. Kim, D. Monllor-Satoca, W. Kim, W. Choi, N-doped TiO_2 nanotubes coated with a thin TaO_xN_y layer for photoelectrochemical water splitting dual bulk and surface modification of photoanodes, *Energy Environ. Sci.* 8 (2014) 247–257.
- [12] S. Hoang, S. Berglund, N. Hahn, A. Bard, C. Mullins, Enhancing visible light photo-oxidation of water with TiO_2 nanowire arrays via cotreatment with H_2 and NH_3 : synergistic effects between Ti^{3+} and N, *J. Am. Chem. Soc.* 134 (2012) 3659–3662.
- [13] J. Wang, D. Tafen, J. Lewis, Z. Hong, A. Manivannan, M. Zhi, M. Li, N. Wu, Origin of photocatalytic activity of nitrogen-doped TiO_2 nanobelts, *J. Am. Chem. Soc.* 131 (2009) 12290–12297.
- [14] R. Asahi, T. Morikawa, T. Ohwaki, K. Aoki, Y. Taga, Visible-light photocatalysis in nitrogen-doped titanium oxides, *Science* 293 (2001) 269–271.
- [15] S. Hoang, S. Guo, N. Hahn, A. Bard, C. Mullins, Visible light driven photoelectrochemical water oxidation on nitrogen-modified TiO_2 nanowires, *Nano Lett.* 12 (2012) 26–32.
- [16] X. Song, W. Li, D. He, H. Wu, Z. Ke, C. Jiang, G. Wang, X. Xiao, The “Midas Touch” transformation of TiO_2 nanowire arrays during visible light photoelectrochemical performance by carbon/nitrogen co-implantation, *Adv. Energy Mater.* (2018) 1800165–1800172.
- [17] S. Liu, L. Yang, S. Xu, S. Luo, Q. Cai, Photocatalytic activities of C-N-doped TiO_2 nanotube array/carbon nanorod composite, *Electrochem. Commun.* 11 (2009) 1748–1751.
- [18] B. Liu, H. Chen, C. Liu, S. Andrews, C. Hahn, P. Yang, Large-scale synthesis of transition-metal-doped TiO_2 nanowires with controllable overpotential, *J. Am. Chem. Soc.* 135 (2013) 9995–9998.
- [19] M. Yang, H. Jha, N. Liu, P. Schmuki, Increased photocurrent response in Nb-doped TiO_2 nanotubes, *J. Mater. Chem.* 21 (2011) 15205–15208.
- [20] M. Xu, P. Da, H. Wu, D. Zhao, G. Zheng, Controlled Sn-doping in TiO_2 nanowire photoanodes with enhanced photoelectrochemical conversion, *Nano Lett.* 12 (2012) 1503–1508.
- [21] C. Wang, Z. Chen, H. Jin, C. Cao, J. Li, Z. Mi, Enhancing visible-light photoelectrochemical water splitting through transition-metal doped TiO_2 nanorod arrays, *J. Mater. Chem. A* 2 (2014) 17820–17827.
- [22] C. Chen, Y. Wei, G. Yuan, Q. Liu, R. Lu, X. Huang, Y. Cao, P. Zhu, Synergistic effect of Si doping and heat treatments enhances the photoelectrochemical water oxidation performance of TiO_2 nanorod arrays, *Adv. Funct. Mater.* (2017) 1701575–1701583.
- [23] D. Schipper, Z. Zhao, A. Leitner, L. Xie, F. Qin, M. Alam, S. Chen, D. Wang, Z. Ren, Z. Wang, J. Bao, K. Whitmire, A $\text{TiO}_2/\text{FeMnP}$ core/shell nanorod array photoanode for efficient photoelectrochemical oxygen evolution, *ACS Nano* 11 (2017) 4051–4059.
- [24] C. Ding, J. Shi, Z. Wang, C. Li, Photoelectrocatalytic water splitting: significance of cocatalysts, electrolyte, and interfaces, *ACS Catal.* 7 (2016) 675–688.
- [25] F. Ning, M. Shao, S. Xu, Y. Fu, R. Zhang, M. Wei, D. v.ans, X. Duan, TiO_2 /graphene/NiFe-layered double hydroxide nanorod array photoanodes for efficient photoelectrochemical water splitting, *Energy Environ. Sci.* 9 (2016) 2633–2643.
- [26] R. Zhang, M. Shao, S. Xu, F. Ning, L. Zhou, M. Wei, Photo-assisted synthesis of zinc-iron layered double hydroxides/ TiO_2 nanoarrays toward highly-efficient photoelectrochemical water splitting, *Nano Energy* 33 (2017) 21–28.
- [27] W. Chen, T. Wang, J. Xue, S. Li, Z. Wang, S. Sun, Cobalt-nickel layered double hydroxides modified on TiO_2 nanotube arrays for highly efficient and stable PEC water splitting, *Small* 13 (2017) 1602420–1602427.
- [28] R. Tang, S. Zhou, Z. Yuan, L. Yin, Metal-organic framework derived $\text{Co}_3\text{O}_4/\text{TiO}_2/\text{Si}$ heterostructured nanorod array photoanodes for efficient photoelectrochemical water oxidation, *Adv. Funct. Mater.* (2017) 1701102–1701113.
- [29] C. Li, T. Wang, Z. Zhao, W. Yang, J. Li, A. Li, Z. Yang, G. Ozin, J. Gong, Promoted fixation of molecular nitrogen with surface oxygen vacancies on plasmon-enhanced TiO_2 photoelectrodes, *Angew. Chem. Int. Ed* 57 (2018) 5278–5282.
- [30] M. Rahman, S. Bazargan, S. Srivastava, X. Wang, M. Abd-Ellah, J. Thomas, N. Heindig, D. Pradhan, K. Leung, Defect-rich decorated TiO_2 nanowires for super-efficient photoelectrochemical water splitting driven by visible light, *Energy Environ. Sci.* 8 (2015) 3363–3373.
- [31] J. Liang, N. Wang, Q. Zhang, B. Liu, X. Kong, C. Wei, D. Zhang, B. Yan, Y. Zhao, X. Zhang, Exploring the mechanism of a pure and amorphous black-blue $\text{TiO}_2\cdot\text{H}$ thin film as a photoanode in water splitting, *Nano Energy* 42 (2017) 151–156.
- [32] Y. Li, J. Wang, X. Liu, C. Shen, K. Xie, B. Wei, Au/ TiO_2 hollow spheres with synergistic effect of plasmonic enhancement and light scattering for improved dye-sensitized solar cells, *ACS Appl. Mater. Interfaces* 9 (2017) 31691–31698.
- [33] S. Wang, Y. Gao, S. Miao, T. Liu, L. Mu, R. Li, F. Fan, C. Li, Positioning the water oxidation reaction sites in plasmonic photocatalysts, *J. Am. Chem. Soc.* 139 (2017) 11771–11778.
- [34] P. Zhang, T. Wang, J. Gong, Mechanistic understanding of the plasmonic enhancement for solar water splitting, *Adv. Mater.* 27 (2015) 5328–5342.
- [35] H. Yin, Y. Kuwahara, K. Mori, H. Cheng, M. Wen, Y. Huo, H. Yamashita, Localized surface plasmon resonances in plasmonic molybdenum tungsten oxide hybrid for visible-light-enhanced catalytic reaction, *J. Phys. Chem. C* 121 (2017) 23531–23540.
- [36] H. Yin, Y. Kuwahara, K. Mori, H. Yamashita, Plasmonic metal/ $\text{Mo}_x\text{W}_{1-x}\text{O}_3$ for visible-light-enhanced H_2 production from ammonia borane, *J. Mater. Chem. A* 6 (2018) 10932–10938.
- [37] S. Park, J. Lee, H. Ko, Transparent and flexible surface-enhanced Raman scattering (SERS) sensors based on gold nanostar arrays embedded in silicon rubber film, *ACS Appl. Mater. Interfaces* 9 (2017) 44088–44095.
- [38] J. Li, W. Zhang, H. Lei, B. Li, Ag nanowire/nanoparticle-decorated MoS_2 monolayers for surface-enhanced Raman scattering applications, *Nano Res.* 11 (2018) 2181–2189.
- [39] Y. Pu, G. Wang, K. Chang, Y. Ling, Y. Lin, B. Fitzmorris, C. Liu, X. Lu, Y. Tong, J. Zhang, Y. Hsu, Y. Li, Au nanostructure-decorated TiO_2 nanowires exhibiting photoactivity across entire UV-visible region for photoelectrochemical water splitting, *Nano Lett.* 13 (2013) 3817–3823.
- [40] Y. Mi, L. Wen, R. Xu, Z. Wang, D. Cao, Y. Fang, Y. Lei, Constructing a AZO/ TiO_2 core/shell nanorod array with uniformly dispersed Au NPs for enhancing photoelectrochemical water splitting, *Adv. Energy Mater.* 6 (2016) 1501496.
- [41] J. Li, S. Cushing, P. Zheng, T. Senty, F. Meng, A. Bristow, A. Manivannan, N. Wu, Solar hydrogen generation by a CdS-Au-TiO_2 sandwich nanorod array enhanced with Au nanoparticle as electron relay and plasmonic photosensitizer, *J. Am. Chem. Soc.* 136 (2014) 8438–8449.
- [42] A. Naldoni, U. Guler, Z. Wang, M. Marelli, F. Malara, X. Meng, L. Besteiro, A. Govorov, A. Kildishev, A. Boltasseva, V. Shalaev, Broadband hot-electron collection for solar water splitting with plasmonic titanium nitride, *Adv. Optical Mater.* 5 (2017) 1601031–1601041.
- [43] M. Chirumamilla, A. Chirumamilla, Y. Yang, A. Roberts, P. Kristensen, K. Chaudhuri, A. Boltasseva, D. Sutherland, S. Bozhevolnyi, K. Pedersen, Large-area ultrabroadband absorber for solar thermophotovoltaics based on 3D titanium nitride nanopillars, *Adv. Optical Mater.* (2017) 1700552–1500559.
- [44] Z. Wang, H. Wang, B. Liu, W. Qiu, J. Zhang, S. Ran, H. Huang, J. Xu, H. Han, D. Chen, G. Shen, Transferable and flexible nanorod-assembled TiO_2 cloths for dye-sensitized solar cells, photodetectors, and photocatalysts, *ACS Nano* 5 (2011) 8412–8419.
- [45] X. Lu, G. Wang, T. Zhai, M. Yu, S. Xie, Y. Ling, C. Liang, Y. Tong, Y. Li, Stabilized TiN nanowire arrays for high-performance and flexible supercapacitors, *Nano Lett.* 12 (2012) 5376–5381.
- [46] T. Zhou, W. Lv, J. Li, G. Zhou, Y. Zhao, S. Fan, B. Liu, B. Li, F. Kang, Q. Yang, Twinborn $\text{TiO}_2\cdot\text{TiN}$ heterostructures enabling smooth trapping-diffusion-conversion of polysulfides towards ultralong life lithium-sulfur batteries, *Energy Environ. Sci.* 10 (2017) 1694–1703.
- [47] Z. Cui, C. Zu, W. Zhou, A. Manthiram, J. Goodenough, Mesoporous titanium nitride-enabled highly stable lithium-sulfur batteries, *Adv. Mater.* 28 (2016) 6926–6931.
- [48] Y. Xie, C. Xia, H. Du, W. Wang, Enhanced electrochemical performance of polyaniline/carbon/titanium nitride nanowire array for flexible supercapacitor, *J. Power Sources* 286 (2015) 561–570.
- [49] M. Jiang, C. Yang, T. Lin, H. Yin, P. Chen, D. Wan, F. Xu, F. Huang, J. Lin, X. Xie, Z. Wang, Visible-light photocatalytic, solar thermal and photoelectrochemical properties of aluminium-reduced black titania, *Energy Environ. Sci.* 6 (2013)

- 3007–3014.
- [50] A. Naldoni, M. Allieta, S. Santangelo, M. Marelli, F. Fabbri, S. Cappelli, C. Bianchi, R. Psaro, V.D. Santo, Effect of nature and location of defects on bandgap narrowing in black TiO₂ nanoparticles, *J. Am. Chem. Soc.* 134 (2012) 7600–7603.
- [51] X. Lv, L. Tao, M. Cao, X. Xiao, M. Wang, Y. Shen, Enhancing photoelectrochemical water oxidation efficiency via self-catalyzed oxygen evolution: a case study on TiO₂, *Nano Energy* 44 (2018) 411–418.
- [52] L. Li, X. Zhang, G. Wu, X. Peng, K. Huo, P.K. Chu, Supercapacitor electrodes based on hierarchical mesoporous MnO_x/nitrided TiO₂ nanorod arrays on carbon fiber paper, *Adv. Mater. Interfaces* 2 (2015) 1400446.
- [53] G. Wang, H. Wang, Y. Ling, Y. Tang, X. Yang, R. Fitzmorris, C. Wang, J. Zhang, Y. Li, Hydrogen-treated TiO₂ nanowire arrays for photoelectrochemical water splitting, *Nano Lett.* 11 (2011) 3026–3033.
- [54] G. Wang, X. Xiao, W. Li, Z. Lin, Z. Zhao, C. Chen, C. Wang, Y. Li, X. Huang, L. Miao, C. Jiang, Y. Huang, X. Duan, Significantly enhanced visible light photoelectrochemical activity in TiO₂ nanowire arrays by nitrogen implantation, *Nano Lett.* 15 (2015) 4692–4698.
- [55] H. Zhang, X. Li, A. Hähnel, V. Naumann, C. Lin, S. Azimi, S.L. Schweizer, A.W. Maijenburg, R.B. Wehrspohn, Bifunctional heterostructure assembly of NiFe LDH nanosheets on NiCoP nanowires for highly efficient and stable overall water splitting, *Adv. Funct. Mater.* (2018) 1706847.
- [56] C. Kim, S. Kim, S.P. Hong, J. Lee, J. Yoon, Effect of doping level of colored TiO₂ nanotube arrays fabricated by electrochemical self-doping on electrochemical properties, *Phys. Chem. Chem. Phys.* 18 (2016) 14370–14375.